Effects of Heat Treatment on Grain-Boundary β-Mg$_{17}$Al$_{12}$ and Fracture Properties of Resistance Spot-Welded AZ80 Mg Alloy

SEYED TIRDAD NIKNEJAD, LEI LIU, TAM NGUYEN, MOK-YOUNG LEE, SHAHRZAD ESMAEILI, and NORMAN Y. ZHOU

The distribution and morphology of β-Mg$_{17}$Al$_{12}$ intermetallic phase in resistance spot-welded AZ80 Mg alloy were investigated by means of optical microscopy, scanning electron microscopy, and X-ray diffraction. The influence of intermetallic phase on mechanical strength was studied by tensile shear testing and fractography. The results showed that continuous networks of β-Mg$_{17}$Al$_{12}$ formed along grain boundaries in both the nugget and heat-affected zone of the spot-welded AZ80 Mg alloy. Those continuous grain-boundary β-Mg$_{17}$Al$_{12}$ networks acted as effective crack propagation paths, which had negative effects on the weld strength. Post-weld solution heat treatment effectively reduced the amount of β-Mg$_{17}$Al$_{12}$ and broke the grain-boundary intermetallic networks in both the nugget and heat-affected zone. This significantly increased the weld strength of AZ80 Mg alloy and changed the fracture mode from nugget pull-out in the as-welded condition to through-thickness after heat treatment.

I. INTRODUCTION

MAGNESIUM alloys have recently been drawing great interest for transportation applications because of their high strength-to-weight ratio. The Mg-Al-Zn alloys known as AZ series are among the most popular Mg alloys. The microstructure and mechanical properties of fusion-welded AZ alloys have been the subject of several recent studies.[1–9] In a nonequilibrium solidification process such as welding, solid solution α-Mg dendrites are formed, depleted in Al (hexagonal-close packed structure) pushing the remaining Al to the interdendritic regions. The solidification is completed by the formation of β-Mg$_{17}$Al$_{12}$ (A12 structure) phase in the interdendritic regions because of a eutectic reaction.[1–4] Meanwhile, in the heat-affected zone (HAZ), grain-boundary (GB) liquation often results in the formation of β- Mg$_{17}$Al$_{12}$ intermetallic phase.[1–4]

It has been suggested that the intragranular precipitation of plate-like β-Mg$_{17}$Al$_{12}$ on the basal plane of hexagonal-close packed α-Mg matrix slightly increased the strength of the AZ alloys. However, the capability of the intergranular β- Mg$_{17}$Al$_{12}$ to increase the strength of bulk Mg materials has been reported to be insignificant.[10–13] In addition, the continuous networks of β-Mg$_{17}$Al$_{12}$ along the GBS greatly reduce the ductility and the fracture toughness of cast Mg-Al alloys.[11,14–17] Heat treatment above the solvus temperature of the Mg-Al binary phase diagram was reported to dissolve the β-Mg$_{17}$Al$_{12}$ phases into the α-Mg matrix leading to a decrease in the strength, but increase in the ductility and fracture toughness.[7,14,15] However, complete dissolution of intergranular β- Mg$_{17}$Al$_{12}$ requires a very long time for the heat treatment of the cast Mg-Al alloys above the solvus temperature (e.g., 693 K (420 °C) for 5 hours[15] and 686 K (413 °C) for 24 hours[17]), which is not an energy-efficient practice. The objectives of the current study are to study the microstructural features of AZ80 magnesium alloy resistance spot welds in the as-welded condition and to examine the effects of partial dissolution of the β-Mg$_{17}$Al$_{12}$ in the fusion zone and HAZ on the mechanical properties of the welds.

II. EXPERIMENTAL PROCEDURE

The material used in the current study was 2-mm-thick commercial-grade hot-rolled sheets of AZ80 (7.7 wt pct Al, 0.7 wt pct Zn, 0.2 wt pct Mn). Rectangular specimens of 100 mm × 25 mm were prepared with the rolling direction (RD) aligned along the longer side according to AWS-D17.2 (see Figure 1(a)). The surfaces of the sheets were chemically cleaned, using a solution of 2.5 g chromic oxide and 100 mL distilled water before welding. Resistance spot welding was performed using a mid-frequency DC resistance spot-welding machine. The optimized welding parameters 26 kA welding current, 8 cycles welding time, and 4 kN welding force were selected based on the maximum strength of the weld nugget and prevention of expulsion during the welding process.[5] Post-weld heat treatment was performed above the solvus temperature of Mg-8 wt pct Al alloy

SEYED TIRDAD NIKNEJAD, Ph.D. Student, SHAHRZAD ESMAEILI, Associate Professor, and NORMAN Y. ZHOU, Professor, are with the Department of Mechanical Engineering, University of Waterloo, Waterloo, ON N2L 3G1, Canada. Contact e-mail: snikneja@uwaterloo.ca LEI LIU, Assistant Professor, is with the Department of Mechanical Engineering, Tsinghua University, Beijing 100084, P.R. China. TAM NGUYEN, Assistant Professor, is with the Canestoga College, Kitchener, ON N2G 4M4 Canada. MOK-YOUNG LEE, Researcher, is with the Research Institute of Industrial Science & Technology (RIST), Pohang 790-330, Republic of Korea.
Manuscript submitted August 29, 2012.
Article published online April 18, 2013

at 673 K (400 °C) for 0.5 hours followed by cooling in the air. Microstructures of the weld samples were examined by optical microscopy (OM) and scanning electron microscopy (SEM) after etching with a solution made 4.2 g picric acid, 10 mL acetic acid, 70 mL ethanol, and 10 mL water. A LEO 1550 scanning microscope equipped with a microanalysis system by energy-dispersive spectroscopy (EDS) was used. X-ray diffraction analysis was performed using Rigaku AFC-8 diffractometer with Cu-Kα X-ray generated by 50-kV acceleration voltage and 40 mA current. The micro-hardness profiles of the welds were measured on the cross sections using a HMV-2000 Vickers micro-hardness apparatus. Testing was performed with 100 g force and a holding time of 15 seconds. Three tensile shear specimens each were prepared for the as-welded and the heat-treated conditions, to evaluate the mechanical properties (Figure 1(a)). The fracture surfaces of the tensile shear samples were afterward studied by SEM. To study the crack propagation path, the tensile testing was stopped immediately after the maximum load was reached (see Figure 1(b)). The crack-bearing specimens were afterward examined by the OM and SEM to investigate the location and the causes of crack formation. The fracture surfaces of the tensile-tested sample were further analyzed by SEM.
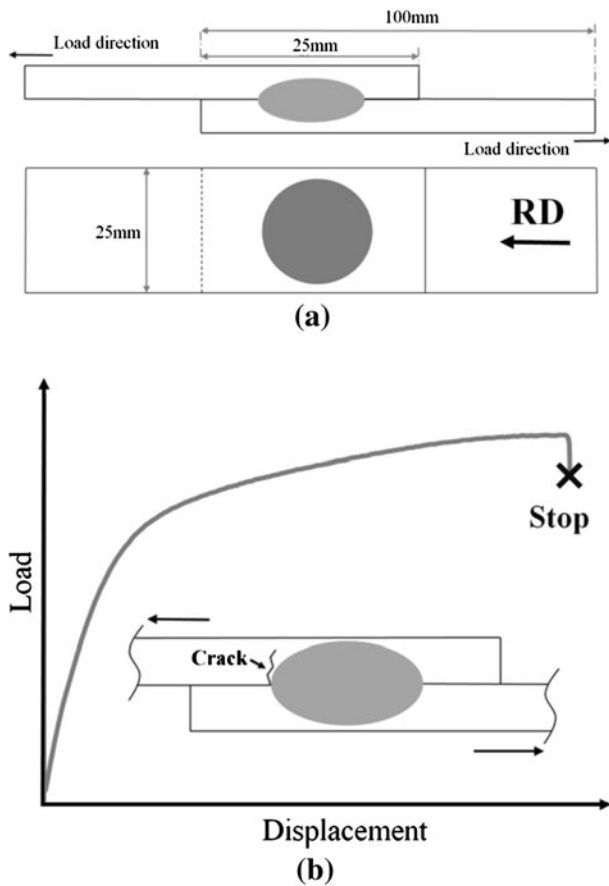

Fig. 1—(a) Scheme of RSW specimens. (b) Scheme of the tensile shear test procedure for assessment of the crack location.

III. RESULTS

A. *Microstructural Characterization across the Weld Zones*

The base metal microstructure of the AZ80 Mg alloy is shown in Figure 2. Fine spherical particles (white) were distributed both within the grains and along the GBs, which according to the EDS results were enriched with Al and identified as β-$Mg_{17}Al_{12}$ phase (see composition of P1 in Table I). Apparently, the eutectic β-$Mg_{17}Al_{12}$ precipitates were formed during the sheet metal casting and hot-rolling processes because of the presence of Al in excess of its solid solubility limits in the α-Mg matrix.[18]

Figures 3(a) and (b) shows the typical microstructure of the fusion zone (nugget). In the as-welded condition, the β-$Mg_{17}Al_{12}$ particles (the white phase in Figure 3(b)) were observed to be mainly distributed along the interdendritic regions in the form of continuous networks. During solidification, the β-$Mg_{17}Al_{12}$ phase was formed because of the eutectic reaction.

Figures 3(c) and (d) illustrate the microstructure of the HAZ. The large particles observed at the fusion boundary (P4 in Figure 3(c)) were enriched in Al and Mn (Table I) and identified as Al_8Mn_5. Such particles have been characterized and reported in a previous study on resistance spot weld of AZ31 alloy.[5] In the HAZ, the distribution and morphology of β-$Mg_{17}Al_{12}$ phase were changed from evenly distributed fine spherical particles in the base metal to continuous networks along the GBs (see P5 in Figure 3(d)). The composition of all the highlighted particles in Figure 3 was analyzed using EDS, and the results are listed in Table I.
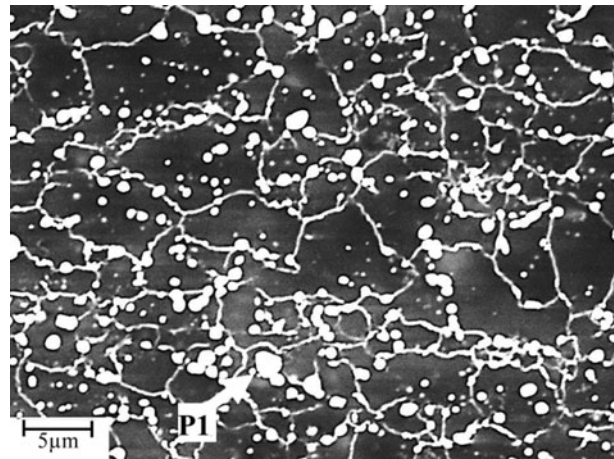

Fig. 2—SEM microstructure of the as-received AZ80 alloy base metal; the EDS analysis results for the highlighted particle are shown in Table I.

Table I. EDS Analysis Results for the Highlighted Particles Shown in Figs. 2 and 3

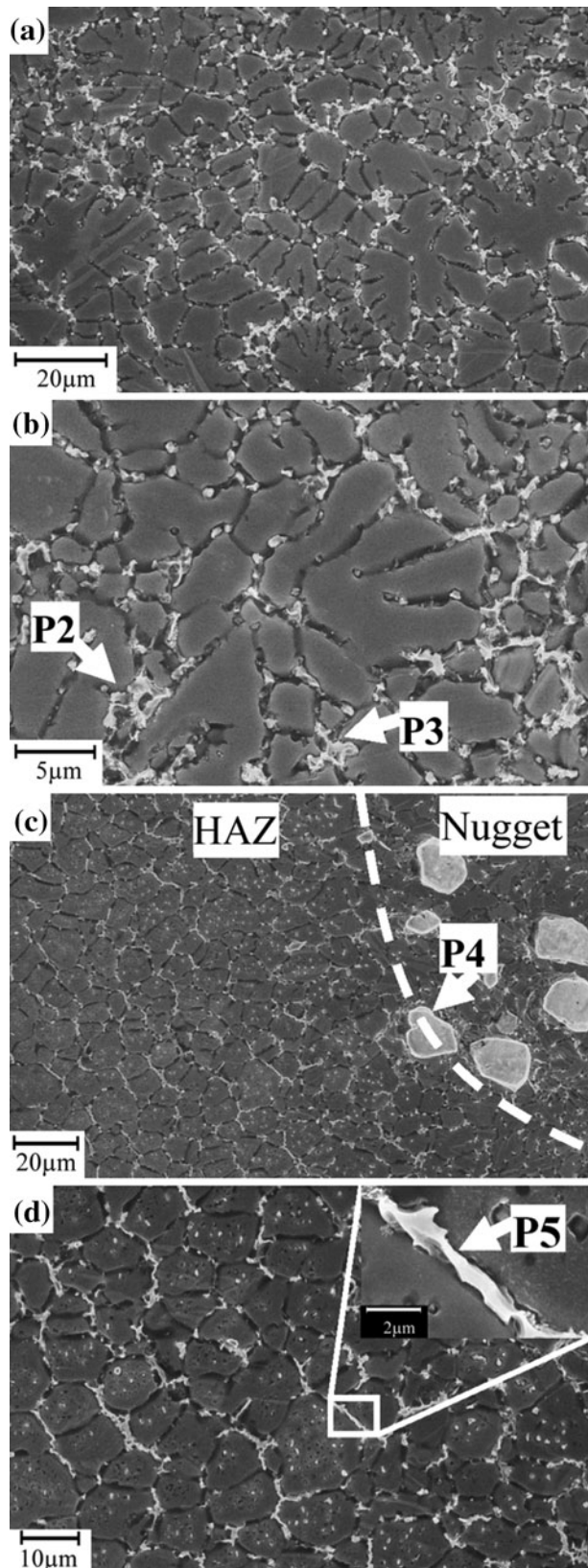| Element	P1	P2	P3	P4	P5
Mg (at. pct)	63.6	64.3	67.3	—	68.4
Al (at. pct)	35.2	34.2	31.4	37.2	30.8
Zn (at. pct)	1.2	1.5	1.3	—	0.8
Mn (at. pct)	—	—	—	62.8	—

Fig. 3—Typical SEM images of the as-welded microstructure: (*a*) Microstructure of the fusion zone. (*b*) High-magnification image from the interdendritic regions. (*c*) Microstructure of HAZ. (*d*) Grain boundary particles in HAZ; the EDS analysis results for the highlighted particles are shown in Table I.

As illustrated by the SEM images of Figure 4, the selected heat treatment partially dissolved the interdendritic β-$Mg_{17}Al_{12}$ phase into the α-Mg matrix in both the HAZ and weld nugget. In the HAZ, the continuous networks of β-$Mg_{17}Al_{12}$ at the GBs were disrupted and changed to irregular shaped β-$Mg_{17}Al_{12}$ (see Figure 4(d)). The average grain in the HAZ of the as-welded samples obtained by the linear intercept method was measured to be 9.2 μm. However, the HAZ average grain size increased to 78.8 μm in the heat-treated samples. In both HAZ and nugget, the sub-micron-sized particles were clearly visible inside the grains. These intragranular particles are believed to be the those pre-existing in the as-welded condition, which did not dissolve into the α-Mg matrix.

X-ray diffraction (XRD) spectra in Figure 5 further confirmed the effect of heat treatment on the dissolution of β-$Mg_{17}Al_{12}$. The XRD results showed the presence of β-$Mg_{17}Al_{12}$ intermetallic compound in both the fusion zone and the HAZ. After heat treatment, the β-$Mg_{17}Al_{12}$ peak intensity of both the fusion zone and the HAZ almost disappeared.

B. Mechanical and Fracture Properties

Table II lists the tensile shear strengths and the fracture modes of the weld nugget in the as-welded and the heat-treated conditions. The strength of the as-welded AZ80 was lower than that of the post-weld heat-treated AZ80. The selected heat treatment increased the strength of the welds by 34 pct. The fracture mode of the AZ80 weld also changed from the nugget pullout of Figure 6(a) to through-thickness failure of Figure 6(b) after the post-weld heat treatment.

To further study the effects of heat treatment on the failure mode and the crack propagation path of AZ80, peak-hold tensile tests as illustrated in Figure 1(b) were conducted. Figure 7(a) shows the typical crack propagation path of an as-welded sample. The crack first initiated from the sharp slit between the two overlapping sheets, then propagated along the fusion line and finally transversed through the HAZ and base metal (see Figure 7(a)). The SEM image of Figure 7(b) shows that the crack path is along the GBs decorated with β-$Mg_{17}Al_{12}$ intermetallic. As indicated by the black and white arrows in Figures 7(c) and (d), secondary microcracks close to the primary crack region were also observed. The black arrows point to microcracks which occurred inside or traversed through the β-$Mg_{17}Al_{12}$ intermetallic, while the white arrows point to micro-cracks at the β-$Mg_{17}Al_{12}$/α-Mg interface.

For the post-weld heat-treated sample, the crack propagated on a different path as illustrated in Figure 8(a). After initiation, the crack propagated along the HAZ/base metal (BM) regions and far away from the fusion boundary. The β-$Mg_{17}Al_{12}$ intermetallic was not observed along the crack paths of the post-weld heat-treated sample (see Figure 8(b)). In addition, high concentrations of twinning were also observed around the crack edges, suggesting that twin deformation of α-Mg matrix was activated after the heat treatment.
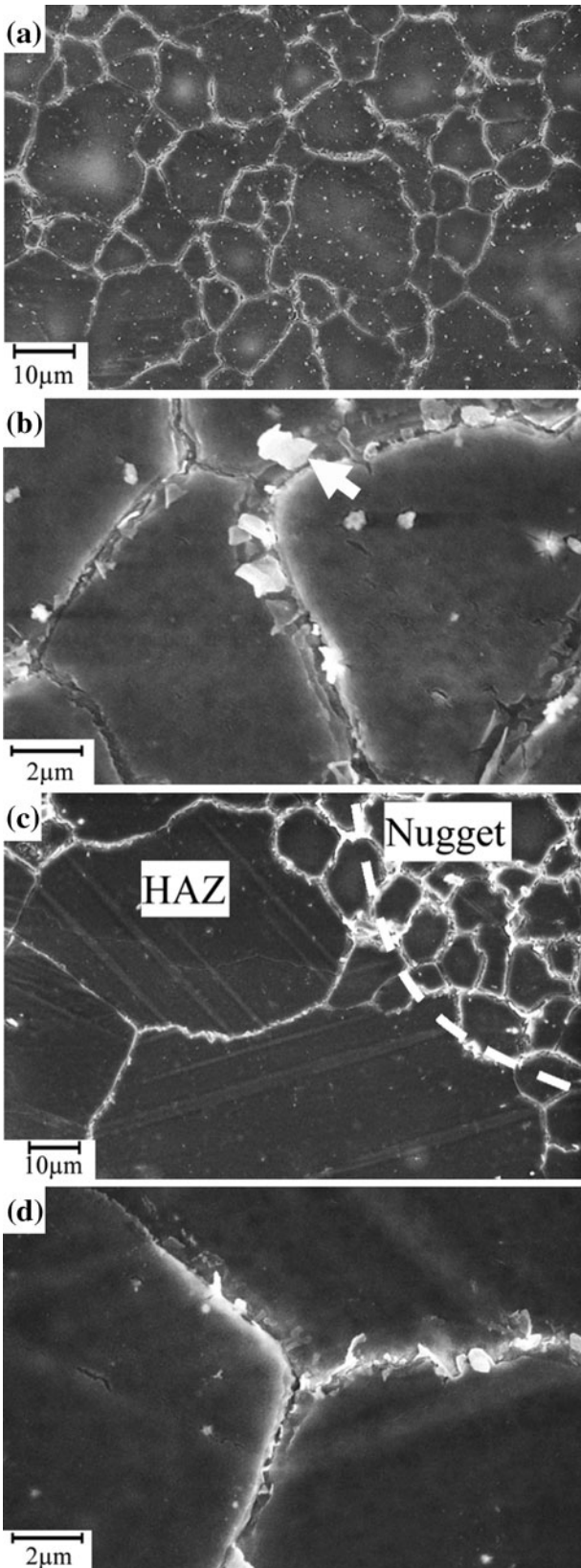
Fig. 4—Typical SEM images of the post-weld heat-treated microstructures: (a) SEM microstructure of fusion zone. (b) Grain boundary particles in fusion zone. (c) SEM microstructure of HAZ. (d) Grain boundary particles in HAZ.
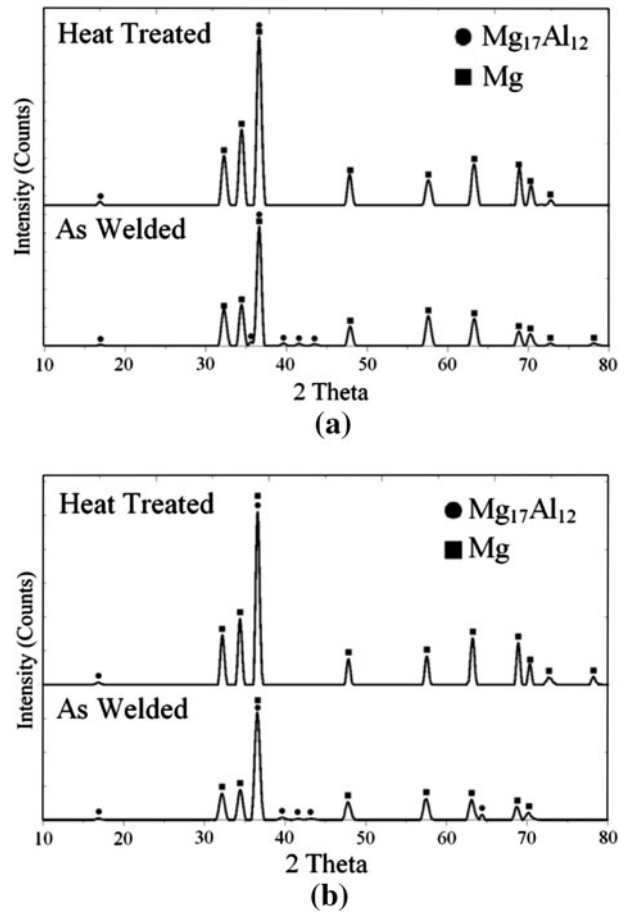

Fig. 5—XRD spectra from (a) Fusion zone. (b) Heat-affected zone.

Table II. Shear Force and Fracture Mode of the Spot Weld Nugget Samples in the As-Welded and Heat Treated Conditions

Strength (kN)		Failure Mode	
As-Welded	Heat Treated	As-Welded	Heat Treated
4.92 ± 0.53	6.63 ± 0.16	nugget pull-out	through-thickness

Figure 9 shows the microhardness profiles across the nugget region from the base metal to the fusion zone in both the as-welded and the post-weld heat-treated conditions. A relatively uniform hardness distribution was detected in the BM, HAZ, and fusion zone (FZ). It was also observed that the hardness of FZ, HAZ, and BM decreased after the heat treatment. Grain growth and partial dissolution of the hard β-$Mg_{17}Al_{12}$ phase after the post-weld heat treatment may have caused the decrease in the hardness.

Figure 10 shows the fracture surface of a tensile specimen in the as-welded condition. Based on the fracture morphology, the fracture surface can be divided into three sections as illustrated in Figure 10(a). Figures 10(b) and (c) shows the low-magnification SEM images of these three sections while Figures 10(d) and
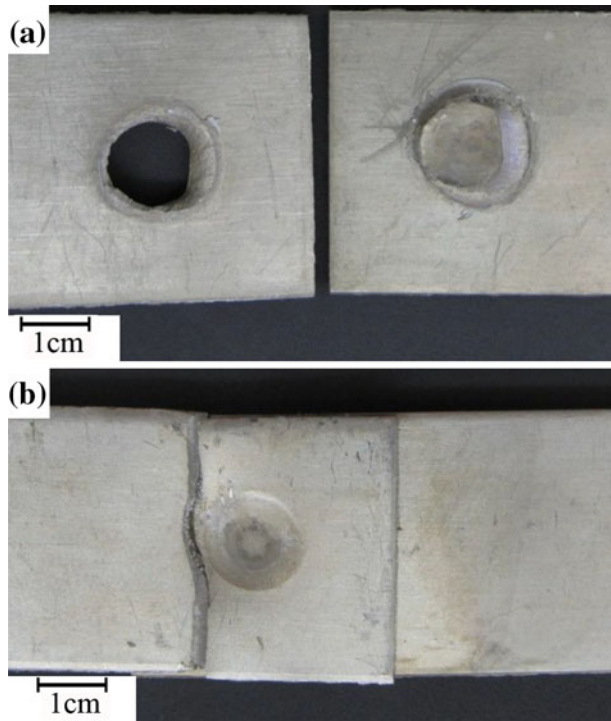
Fig. 6—Illustration of fracture modes: (*a*) Nugget-pullout fracture for the as-welded sample. (*b*) Through-thickness fracture after the post-weld heat treatment.

(e) shows high-magnification images of Sections I and II, respectively.

The Section I was located at the FZ/HAZ interface and appeared to have a dendritic structure (Figure 10(d)), which indicates that very weak joining (or no joining) occurred at the faying surface close to the notch of the nugget. Located in the HAZ, Section II appeared to exhibit cleavage-like steps as shown in low magnification image of Figure 10(b). Close analysis of the fracture surface in Section II revealed a high density of microvoids (Figure 10(e)). In Table III, the EDS analysis results, obtained from the fracture surface of Section II, indicated the presence of β-$Mg_{17}Al_{12}$ particles near the microvoids (P2, P3, and P5). Finally, Section III was the final fracture through the BM, which showed a shear fracture due to over loading. This fracture was associated with the presence of randomly distributed microscopic cracks (Figure 10(c)).

Figure 11 illustrates the fracture surface of the post-weld heat-treated sample. The fracture morphologies were different from those of the as-welded sample. Similar to the previous case, the fracture surface of the post-weld heat-treated sample could be divided into three sections as shown in Figure 11(b), and their locations are schematically illustrated in Figure 11(a). Along the FZ/HAZ interface, the dimple-like morphology fracture surface of the Section I, shown in Figure 11(c), suggests good weld strength. This dimple-like morphology fracture surface was not observed in the Section I of the as-welded sample. The Section II was mostly related to the through-thickness fracture in the HAZ/BM region. The high-magnification SEM image in
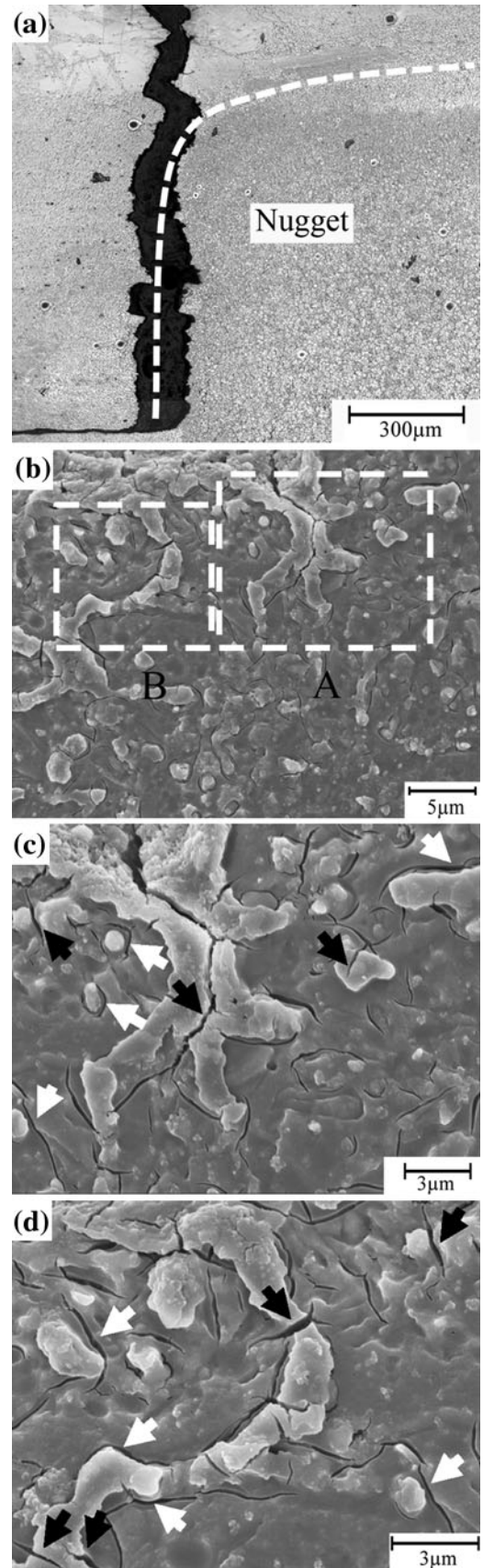

Fig. 7—(*a*) Typical crack propagation path in the as-welded condition. (*b*) Microstructure near the crack region for the as-welded sample. (*c*) Area A at higher magnification. (*d*) Area B at higher magnification.
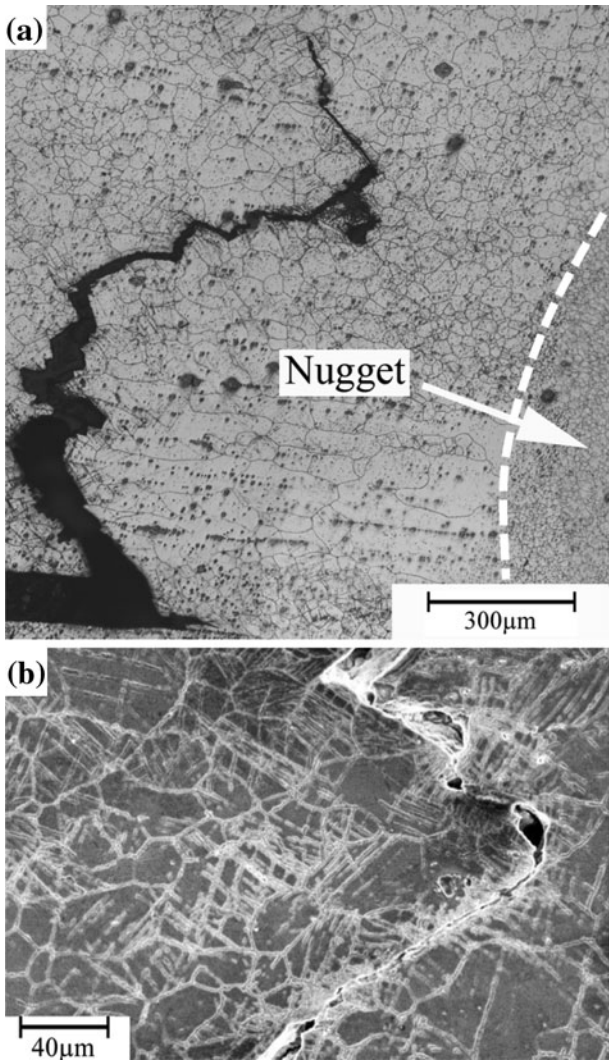
Fig. 8—(a) Typical crack propagation path in the post-weld heat-treated sample. (b) Cross-sectional microstructure near the crack region for the post-weld heat-treated sample.
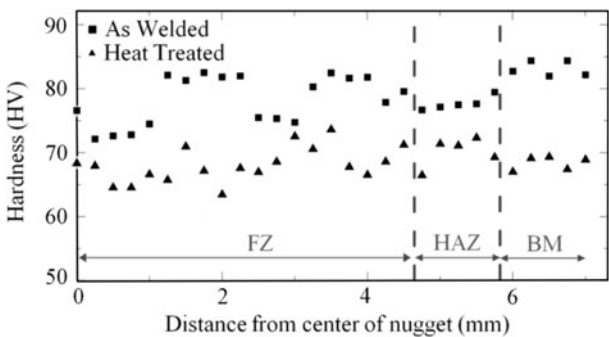

Fig. 9—Microhardness profile across the weld nugget.

Figure 11(d) shows a ductile fracture surface, which is similar to the fracture surface of the as-received AZ80 solution heat treated at 673 K (400 °C) for ½ hr in Figure 11(e). No evidence of Al-rich intermetallic was detected on the fracture surface of post-weld heat-treated sample. Section III showed the same morphology as found in the as-welded sample for the Section III.

IV. DISCUSSION

During the resistance spot welding, the HAZ of the AZ80 spot weld was quickly heated up to greater than the solvus temperature because of the fast heating rate. However, the pre-existing β-$Mg_{17}Al_{12}$ particles at the GBs of the base metal (Figure 2) did not have enough time to dissolve into the α-Mg matrix since their dissolution is controlled by the time–temperature-dependent solid-state diffusion mechanism. On further heating the material in HAZ up to the eutectic temperature (T_E), the remaining β-$Mg_{17}Al_{12}$ reacted with the surrounding α-Mg matrix and formed the eutectic (C_E) liquid film at the GBs (Figure 3(d)). This is also known as GB liquation, a phenomenon that has been observed previously in the HAZ of Al alloys.[19,20] During cooling, the liquid at the GBs formed a continuous network of β-$Mg_{17}Al_{12}$ phase by eutectic reaction.

From fracture mechanics, the sharp slit between the two overlapping metal sheets surrounding a spot weld nugget is an intrinsic three-dimensional crack, which results in a high concentrated local stress.[21–23] Consequently, the crack, presumably, had already been initiated before the tensile shear test, and the resistance to crack propagation controlled the tensile shear strength of the spot weld.

Previous studies have shown that the formation of β-$Mg_{17}Al_{12}$ as continuous networks along the GBs or interdendritic region decreases the toughness and ductility of the as-cast structures.[11,15] As discussed earlier, in AZ80 spot welds, continuous networks of β-$Mg_{17}Al_{12}$ phase formed along the GBs of the HAZ. These continuous GB β-$Mg_{17}Al_{12}$ networks created a preferred path for propagation of the pre-existing crack during the tensile shear test. On the other hand, the interdendritic β-$Mg_{17}Al_{12}$ network inside the fusion zone (Figures 3(a) and (b)) was considered to be a tortuous crack path because of the dendritic nature of this area, which offered more resistance to crack propagation. Also, cracks could grow more easily through the brittle intermetallic-bearing GBs of large grains in the HAZ (Figure 3(d)).

In terms of the as-welded microstructure near the crack region (see Figures 7(c) and (d)), the crack could easily propagate by coalescing microvoids/cracks, which were formed by two distinctive mechanisms:

A. Intrinsic Fracture of Intermetallics

As indicated by black arrows in Figures 7(c) and (d), the intermetallics were ideal sites for crack initiation and propagation. When the Mg-Al intermetallic compound grew too thick, it became significantly brittle. A similar phenomenon has previously been observed in Mg-to-Al dissimilar welds.[24,25] The presence of a hard brittle second phase in the GBs of soft solute-depleted matrix was reported to deteriorate the mechanical properties in HAZ.[10] Under tensile loading, the depleted matrix

(a)

(b)

200μm

(c)

100μm

(d)

20μm

(e)

20μm
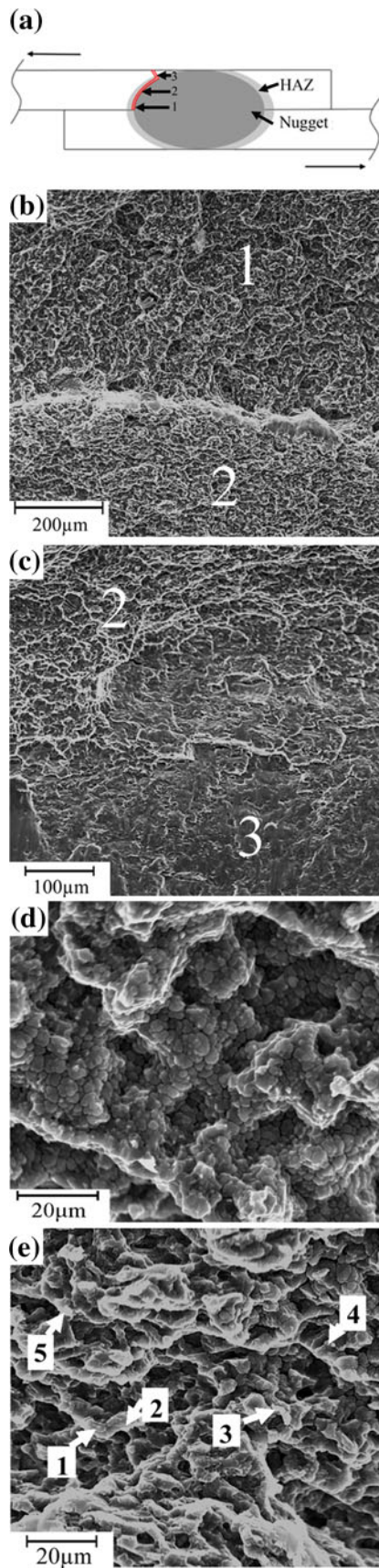
◄Fig. 10—Fracture surface of the spot weld sample in the as-welded condition: (*a*) Scheme of the fracture location showing three sections. I and II. (*b*) Fracture surface in Sects. I and II. (*c*) Fracture surface in Sects. II and III. (*d*) High-magnification image of fracture surface in Sect. I. (*e*) High-magnification image of fracture surface in Sect. II.

Table III. EDS Analysis Results for the Particles Shown in Fig. 10(e)

| Particles	1	2	3	4	5
Mg (at. pct)	84.6	83.5	82.5	81.5	77.6
Al (at. pct)	15.4	16.5	17.5	18.5	22.4

simply yielded without much resistance, while the second intermetallic phase fractured.[19]

B. Detachment of Matrix and Particle at the Interface

Aluminum has been reported as an efficient solid-solution-strengthening alloying element in α-Mg microstructure.[9] The formation of GB β-$Mg_{17}Al_{12}$ in the HAZ of AZ80 depleted the surrounding regions of solute and hence softened the material.[9] Therefore, the Al-depleted regions as shown by the white arrows in Figures 7(c) and (d) were suitable places for microvoid formation during the tensile shear test. Crack initiation in the β-$Mg_{17}Al_{12}$/α-Mg interface was previously reported in different cast structures such as tensile-tested AZ91 alloy,[11] forged homogenized AZ80 alloy[26], and vibration-failed AZ31.[27] The nucleation of a microscopic void/crack around second-phase particles occured during the tensile shear testing when the internal stresses exceeded the adhesive strength of the particle/matrix interface. When this critical stress value was reached, void/crack nucleation was favored to occur. The β-$Mg_{17}Al_{12}$ particles were detected near the microvoids on the fracture surface of the as-welded sample shown in Figure 10(e).

From the above mechanisms, microvoids/cracks could either initiate within the brittle Mg-Al intermetallics, or first initiate in the Al-depleted region and then traverse through the Mg-Al intermetallics. The resistance-to-crack propagation in a material consisting of a ductile matrix and brittle secondary-phase particles is severely weakened by the coalescence of microvoids/cracks.[28] As a consequence, the as-welded condition offers little resistance to crack propagation, and thus a low tensile shear strength.

In the current study, continuous HAZ GB β-$Mg_{17}Al_{12}$ networks had severe adverse effects on the weld strength. In the as-welded condition, the crack propagated either along the $Mg_{17}Al_{12}$/α-Mg interface or through the brittle fracture of the $Mg_{17}Al_{12}$ particles. Facing little or no lattice resistance, twinning did not appear near the crack region (Figure 7(a)). On the contrary, the absence of continuous GB β-$Mg_{17}Al_{12}$ networks in the solution-heat-treated material caused a
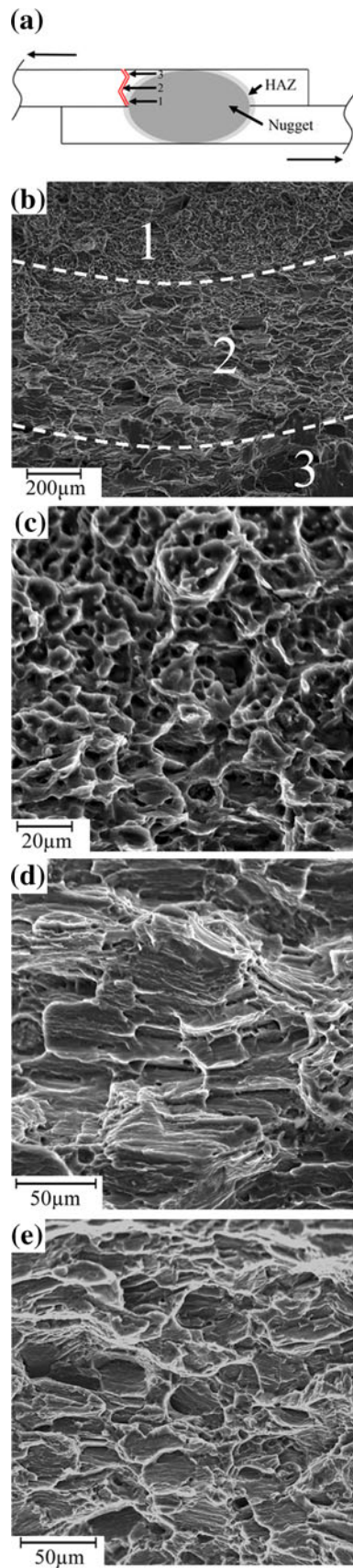
Fig. 11—Fracture surface of the spot weld region in the heat-treated condition: (a) Scheme of the fracture location. (b) Fracture surface in Sects. I, II, and III. (c) High-magnification image of fracture surface in Sect. I. (d) High-magnification image of fracture surface in Sect. II. (e) Fracture surface in the AZ80 base metal in heat-treated condition.

significant change in fracture behavior. In the latter case, crack propagation was associated with extensive energy-consuming twinning near the crack tip (see Figure 8(b)). Thus, in the absence of GB β-$Mg_{17}Al_{12}$, the lattice structure resisted against crack propagation by undergoing significant twinning before fracture. The formation of twins along the crack tip was previously reported in the tensile testing of the heat-treated AZ cast alloys.[14,29]

Solution-heat treatment dissolved a high fraction of the GB β-$Mg_{17}Al_{12}$ phase and therefore caused an increased level of solid-solution strengthening. Although solution treatment also induced considerable grain growth in the both HAZ and BM, softening due to the Hall–Petch effect appeared to be small or partially compensated by solid-solution strengthening. Such behavior may be attributed to twinning-modified Hall–Petch effect[30] and potential twin-induced hardening.[31] The prevalence of twinning mechanism in the HAZ of the solution-treated sample is supported by the observation reported in Figure 8(b), as well as the well-established reports on the dominance of twinning deformation mechanism in coarse-grained magnesium.[30–32] The enhanced twinning mechanism, due to grain growth, is able to accommodate strain during plastic deformation and thus improve ductility.[33] It is worth mentioning that tensile test of the as-received and the heat-treated (673 K for 0.5 hours) AZ80 BM has also been carried out along the rolling direction. It has been found that the elongation to failure increased from 8 pct in the as-received condition to 25 pct in the heat-treated condition. Such improvement in the ductility of the coarse-grained microstructure can be considered as the resistance-to-crack propagation during tensile shear testing of the heat-treated weld samples.

The evolution of texture characteristics as a result of welding and/or post-weld heat treatment has not been investigated as part of the current study. It is generally understood that AZ-type alloys take up a strong basal texture during conventional hot-and cold-deformation processes, and weakening this texture improves ductility.[34] It has also been reported that static recrystallization of a hot-rolled AZ31 alloy upon subsequent annealing at 573 K occurred in 90 seconds, and further annealing for 4 minutes led to a significant reduction in the maximum intensity of basal texture. However, the extension of annealing for longer times (i.e., ≥10 minutes) resulted in the reversal of basal texture weakening.[35] Grain coarsening and abnormal grain growth were reported to occur concurrent by the texture reversal during annealing of the hot-rolled AZ31 alloy.[35] Considering the reported similarities in texture evolution of AZ80 and AZ31 alloys,[36–38] the prolonged heat treatment at 673 K (400 °C), and the observed

significant grain growth in the heat-treated sample, it is expected that texture improvement due to the current post-weld heat treatment is insignificant, if at all.

The β-$Mg_{17}Al_{12}$ particles on the fracture surface of the as-welded sample (see Figure 10(e)) indicated that those particles were responsible for the microvoid nucleation during the tensile shear test. It was previously reported that the β-$Mg_{17}Al_{12}$ brittle particles nucleated microvoids and microcracks in tensile testing because of stress concentration.[39–41] The lack of microvoids on the fracture surface of the heat-treated tensile shear samples indicated a change in the fracture mode. Fracture appearance became more similar to ductile fracture observed in the BM (Figure 11(e)). Similar observations of fracture surface made in AZ31 alloy suggested a good ductility, as well.[42,43] The fracture morphology of the post-weld heat-treated sample in Figure 11(d) was coarser than that of the solution heat treated BM of Figure 11(e), which was consistent with the larger grain size of the heat-treated HAZ/BM microstructure compared with the as-received BM. In other words, after heat treatment, the AZ80 spot welds showed a more ductile fracture surface and the Al-rich intermetallic compounds were no longer seen on the fracture surfaces.

V. CONCLUSIONS

The major conclusions of this study can be summarized as follows:

1. After resistance spot welding, the morphology and distribution of β-$Mg_{17}Al_{12}$ in AZ80 alloy changed from the uniformly distributed fine spherical particles to continuous networks along grain boundaries in both the weld nugget and HAZ.
2. The peak-hold tensile shear test showed that the continuous grain boundary β-$Mg_{17}Al_{12}$ intermetallic networks provided effective crack propagation paths which had negative effects on the weld strength.
3. A short post-weld solution heat treatment did not completely dissolve the HAZ grain-boundary intermetallics, but effectively broke the network and eliminated the suitable crack propagation path during tensile shear testing.
4. After the partial solution heat treatment, the weld strength increased by 34 pct because of the disappearance of grain-boundary β-$Mg_{17}Al_{12}$ networks. A high density of twinning was observed in the post-weld heat-treated sample, and the fracture mode changed from nugget pull-out to through-thickness failure.

REFERENCES

1. S.F. Su, J.C. Huang, H.K. Lin, and N.J. Ho: *Metall. Mater. Trans. A*, 2001, vol. 33A, pp. 1461–73.
2. D.X. Sun, D.Q. Sun, X.Y. Guand, and Z.Z. Xuan: *ISIJ Int.*, 2008, vol. 49, pp. 270–74.
3. C.J. Huang, C.M. Cheng, C.P. Chouand, and F.H. Chen: *J. Mater. Sci. Technol.*, 2011, vol. 27, pp. 633–40.
4. X. Cao, M. Jahazi, J.P. Immarigeon, and W. Wallace: *Mater. Process. Technol.*, 2006, vol. 171, pp. 188–204.
5. L. Xiao, L. Liu, Y. Zhou, and S. Esmaeili: *Metall. Mater. Trans. A*, 2010, vol. 41A, pp. 1511–22.
6. L. Liu, L. Xiao, J.C. Feng, Y.H. Tian, S.Q. Zhou, and Y. Zhou: *Metall. Mater. Trans. A*, 2010, vol. 41A, pp. 2642–50.
7. Y. Wang, G. Liu, and Z. Fan: *Scripta Mater.*, 2006, vol. 54, pp. 903–08.
8. T. Zhu, Z.W. Chen, and W. Gao: *Mater. Charact.*, 2008, vol. 59, pp. 1550–58.
9. K.N. Braszczynska-Malik and M. Mroz: *J. Alloys Compd.*, 2011, vol. 509, pp. 9951–58.
10. G. Nussbaum, P. Sainfort, and G. Regazzoni: *Scripta Metall. Mater.*, 1989, vol. 23, pp. 1079–84.
11. Y.Z. Lu, Q.D. Wang, W.J. Ding, X.Q. Zeng, and Y.P. Zhu: *Mater. Lett.*, 2000, vol. 44, pp. 265–68.
12. S. Celotto: *Acta Mater.*, 2000, vol. 48, pp. 1775–87.
13. J.B. Clark: *Acta Metall. Mater.*, 1968, vol. 16, pp. 141–52.
14. S. Kleiner, O. Beffort, A. Wahlen, and P.J. Uggowitzer: *Light Met.*, 2002, vol. 2, pp. 277–80.
15. I.A. Yakubtsov, B.J. Diak, C.A. Sager, B. Bhattacharya, W.D. MacDonald, and M. Niewczas: *Mater. Sci. Eng., A*, 2008, vol. 496, pp. 247–55.
16. L.A. Dobrzanski, T. Tanski, L. Cizek, and Z. Brytan: *J. Mater. Process. Technol.*, 2007, vol. 192, pp. 567–74.
17. M.M. Avedesian and H. Baker: *Magnesium and Magnesium Alloys*, ASM International, Materials Park, OH, 1999, p. 79.
18. M. Hansen and K. Anderko: *Constitution of Binary Alloys*, 2nd ed., McGraw-Hill, New York, NY, 1958, p. 1042.
19. C. Huang and S. Kou: *Weld. J.*, 2000, vol. 5, pp. 113–20.
20. C. Huang and S. Kou: *Weld. J.*, 2002, vol. 10, pp. 211–22.
21. S. Zhang: *Inter. J. Fract.*, 1997, vol. 88, pp. 167–85.
22. J.F. Copper and R.A. Smith: *Int. J. Fatig.*, 1985, vol. 3, pp. 137–40.
23. N. Pan and S.D. Sheppard: *Eng. Fract. Mech.*, 2003, vol. 70, pp. 671–84.
24. P. Liu, Y. Li, H. Geng, and J. Wang: *Mater. Lett.*, 2007, vol. 61, pp. 2001–05.
25. P. Liu, Y. Li, H. Geng, and J. Wang: *Mater. Lett.*, 2005, vol. 59, pp. 2001–05.
26. Q. Guo, H. Yan, Z. Chen, and H. Zhang: *Trans. Nonferr. Met. Soc.*, 2006, vol. 16, pp. 922–26.
27. J.M. Song, T.S. Lui, H.W. Chang, and L.H. Chen: *Scripta Mater.*, 2006, vol. 54, pp. 399–404.
28. S. Kou: *Welding Metallurgy*, 2nd ed., John Wiley & Sons, Hoboken, NJ, 2003, p. 328.
29. B. Kim, J. Do, S. Lee, and I. Park: *Mater. Sci. Eng., A*, 2010, vol. 527, pp. 6745–57.
30. M.R. Barnett: *Scripta Mater.*, 2008, vol. 59, pp. 696–98.
31. M.R. Barnett, Z. Keshavarz, A.G. Beer, and D. Atwell: *Acta Mater.*, 2004, vol. 52, pp. 5093–5103.
32. M.A. Meyers, O. Vohringer, and V.A. Lubarda: *Acta Mater.*, 2001, vol. 49, pp. 4025–39.
33. H. Zhang, G.S. Huang, B. Song, L. Zhang, and D.Q. Kong: *Trans. Nonferr. Metal. Soc.*, 2011, vol. 21, pp. 844–850.
34. T. Mukai, M. Yamanoi, H. Watanabe, and K. Higashi: *Scripta Mater.*, 2001, vol. 45, pp. 89–94.
35. M. Sanjari, S.F. Farzadfar, T. Sakai, H. Utsunomiya, E. Essadiqi, I.H. Jung, and S. Yue: *Mater. Sci. Eng., A*, 2013, vol. 561, pp. 191–202.
36. P. Mehrotra, T.M. Lillo, and S.R. Agnew: *Scripta Mater.*, 2006, vol. 55, pp. 855–58.
37. S.R. Agnew, P. Mehrotra, T.M. Lillo, G.M. Stoica, and P.K. Liaw: *Acta Mater.*, 2005, vol. 53, pp. 3135–46.
38. S.R. Agnew, P. Mehrotra, T.M. Lillo, G.M. Stoica, and P.K. Liaw: *Mater. Sci. Eng., A*, 2005, vol. 408, pp. 72–78.
39. Z. Wang, M. Gao, H. Tang, and X. Zeng: *Mater. Charact.*, 2011, vol. 62, pp. 943–51.

40. O. Sabokpa, A. Zarei-Hanzaki, and H.R. Abedi: *Mater. Sci. Eng., A*, 2012, vol. 550, pp. 31–38.
41. H.A. Patel, D.L. Chen, S.D. Bhole, and K. Sadayappan: *J. Alloys Compd.*, 2010, vol. 496, pp. 140–48.
42. P.B. Srinivasan, S. Riekehr, C. Blawert, W. Dietzel, and M. Kocak: *T. Nonferr. Metal. Soc.*, 2011, vol. 21, pp. 1–8.
43. M. Bobby Kannan, W. Dietzel, C. Blawert, C. Riekehr, and M. Kocak: *Mater. Sci. Eng., A*, 2007, vol. 444, pp. 220–26.